water

MDPI

Article

Fabrication of Manganese-Supported Activated Alumina Adsorbent for Defluoridation of Water: A Kinetics and Thermodynamics Study

Kun You [1], Peijie Li [2], Jinxiang Fu [1], Ning Kang [1], Yujia Gao [1], Xiaoxiang Cheng [2,*], Yuehong Yang [3] and Furui Yu [3]

[1] School of Municipal and Environmental Engineering, Shenyang Jianzhu University, Shenyang 110168, China; youkun1978@163.com (K.Y.); fujinxiang@sina.com (J.F.); kangning2552@163.com (N.K.); gyy891212@163.com (Y.G.)
[2] School of Municipal and Environmental Engineering, Shandong Jianzhu University, Jinan 250101, China; 17865161758@163.com
[3] Shandong Urban Construction Vocational College, Jinan 250103, China; nataliejune@163.com (Y.Y.); wuyufzfr@163.com (F.Y.)
* Correspondence: cxx19890823@163.com

Abstract: Fluoride pollution frequently occurs in many underground drinking water sources due to discrepancies in the geological environment. To address this problem, a manganese-supported activated alumina (MnOOH-supported AA) adsorbent was proposed in the present study. The adsorbent was prepared with an impregnation method, then the morphology and microstructure were systematically characterized. Further, the adsorption kinetics and thermodynamics were systematically explored through static experiments to confirm the adsorption mechanism. The results showed that MnOOH was successfully loaded on the activated alumina (AA), and irregular and convex spinous structures were formed on the surface of particles. Compared with the AA, MnOOH-supported AA exhibited a significantly higher defluoridation rate, which has been doubled. The kinetic behavior of fluoride adsorption on MnOOH-supported AA was governed by the quasi-second-order kinetics model with regression coefficients of 0.9862, 0.9978 and 0.9956, respectively. The adsorption rate was mainly ascribed to the intra-particle diffusion. Additionally, the Freundlich isotherm equation fitted the adsorption thermodynamic process reasonably well compared with the Langmuir adsorption model. Specifically, the correlation coefficients were 0.9614, 0.9383 and 0.9852 at 25 °C, 35 °C and 45 °C, respectively. The adsorption–desorption isotherm plot was similar to the Type V isotherm. The whole fluoride adsorption was a spontaneous endothermic reaction, and controlled by chemical adsorption. These results demonstrated that MnOOH-supported AA as an alternative to the conventional AA showed promising potential for defluoridation in drinking water treatment.

Keywords: manganese-supported activated alumina (MnOOH-supported AA); fluoride; kinetics; thermodynamics

check for updates

Citation: You, K.; Li, P.; Fu, J.; Kang, N.; Gao, Y.; Cheng, X.; Yang, Y.; Yu, F. Fabrication of Manganese-Supported Activated Alumina Adsorbent for Defluoridation of Water: A Kinetics and Thermodynamics Study. *Water* **2021**, *13*, 1219. https://doi.org/10.3390/w13091219

Academic Editor: An Ding

Received: 20 March 2021
Accepted: 24 April 2021
Published: 28 April 2021

Publisher's Note: MDPI stays neutral with regard to jurisdictional claims in published maps and institutional affiliations.

Copyright: © 2021 by the authors. Licensee MDPI, Basel, Switzerland. This article is an open access article distributed under the terms and conditions of the Creative Commons Attribution (CC BY) license (https://creativecommons.org/licenses/by/4.0/).

1. Introduction

China has abundant groundwater resources, accounting for 30% of the total water resources. Due to stable water temperature, simple water-supply facilities, reliable water-supply capacity, favorable water quality and extensive distribution etc., the groundwater is being developed on a large scale and has been a vital source of drinking water. However, the water quality and safety cannot be guaranteed for nearly half of the groundwater. The water could be polluted by fluoride because of human production activities and natural geochemical processes. Long-term use of high-fluoride water will do harm to human health, causing endemic fluorosis such as dental fluorosis and skeletal fluorosis. The intelligence quotient of children could be significantly affected if excessive fluoride is ingested [1,2]. In China (Figure S1), high-fluoride shallow groundwater is mainly distributed in Heilong

Jiang, Jilin, Liaoning, Shanxi, Jiangsu, Ningxia and Gansu Provinces, etc. The fluoride content in groundwater is 2~5 mg/L, and sometimes even as high as 10 mg/L. Meanwhile, the phenomenon of high iron ions generally occurs in Heilong Jiang, Jilin, Liaoning, Shandong, Hubei and Hebei Provinces and the Nei Monggol Autonomous Region, etc. It is noteworthy that groundwater is a significant drinking water source in northern rural areas of China. In general, the occurrence of high-fluoride and high-iron are noticed depending on the geological structure. However, due to the local geological structure and economic environment conditions, there is still a lack of effective defluoridation measures in many rural areas. Therefore, there is an urgent technical demand by livelihood problems to relieve fluoride pollution.

At present, there are five major types of commonly used fluoride removal methods: precipitation [3–5], ion exchange [6,7], membrane filtration [8,9], electrodialysis [10] and adsorption [11,12], all of which have their own advantages and shortcomings, as shown in Table 1. Among these methods, adsorption is widely applied for low operating costs and simple operation process [13], and the most frequently used adsorbents include activated alumina (AA), zeolite and chitosan [14,15]; among these, AA is the most commonly used. Table 2 shows the related research on adsorbents and adsorption effects abroad. Although the common adsorbents exhibit preferable adsorption capacity, there are still problems occurring in defluoridation, including low saturation adsorption capacity and increasing amounts of adsorbent dosage [16]. Recently, fabricating adsorbents coated with Ca, Zr, La, Ce, Mn and other elements have attracted increasing attention for fluoride removal, and the modified adsorbents have exhibited excellent removal. Calcium hydroxide used for fluoride removal could produce sludge with a high water content and an unstable fluoride concentration in the effluent. It is reported that manganese oxide (MnOOH) with a large surface area and microporous structure [17–19] is prevalent in epigenetic geochemical environments, which manifests excellent adsorption performance for anions [20]. At present, there are few studies related to AA loaded with MnOOH for fluoride removal in groundwater.

In the present study, a manganese-supported AA (MnOOH-supported AA) adsorbent was evaluated for defluoridation from aqueous solutions. To be specific, AA with a size of 3~5 mm was selected, and MnOOH was loaded on AA using an impregnation method. The morphology and microstructure of MnOOH-supported AA were analyzed using various characteristic means. Moreover, the adsorption kinetics and adsorption thermodynamics were determined by a quasi-first-order model, a quasi-second-order model, the Weber and Morris model, the Freundlich isotherm equation and the Langmuir isotherm equation. The adsorption mechanism was then discussed on the strength of the experimental results.

Table 1. Comparative analysis of fluoride removal methods.

Technique	Category	Materials	Advantages	Limitations
Precipitation	Chemical precipitation	Calcium salt, etc.	Low cost, simple operation	High amount of retained water (sludge dewatering is required prior to disposal)
	Coagulant sedimentation	Iron salt, aluminum salt, etc.	Low cost, simple operation	Can be expensive, efficiency depends on pH and the presence of co-existing ions in water, adjustment and readjustment of pH is required, elevated residual aluminum concentration, formation of sludge with a high amount of toxic aluminum fluoride complex
Ion exchange	Ion exchange	Ion exchange resin	High efficiency	High cost of installation and regeneration
Separation membrane	Electrodialysis	Ion exchange membrane	High efficiency, no need to dosage agents	Expensive, vulnerable to interfering ions (sulfate, phosphate, chloride, bicarbonate, etc.), high operation cost, toxic concentrate generated
	Reverse osmosis	Reverse osmosis membrane	High efficiency, suitable for treating high-fluoride water	High cost of installation and maintenance, replacement of media after multiple regenerations
	Ultrafiltration	Ultrafiltration membrane	No risk of secondary contamination, suitable for treating high-fluoride water	High cost, pre-processing complexity, strict technical requirements
	Nanofiltration	Nanofiltration membrane		
Adsorption	Activated alumina	Activated alumina	Greater accessibility, low cost, simple operation, availability of wide range of adsorbents, produce high-quality water, environmentally friendly	Common ions interfere with fluoride adsorption, regeneration difficult, low adsorption efficiency under high fluoride concentration

Table 2. A summary of various adsorbents for fluoride removal from water.

S. No.	Adsorbent	Adsorption Capacity	Concentration Range	Contact Time	pH
1	Fe-impregnated chitosan (Fe-CTS)	1.97 mg/g	10 mg/L	6 h	-
2	Magnetic iron oxide fabricated hydrotalcite/chitosan (Fe_3O_4HTCS)	5.03 mg/g	10 mg/L	20 min	5
3	Hydrous zirconium oxide-impregnated chitosan beads	22.1 mg/g	9.7–369.2 mg/L	160 h	5
4	Sn(IV) chloride impregnated chitosan La^{3+} modified	17.63 mg/g	5–100 mg/L	30 min	6
5	Lanthanum-aluminum loaded hydrothermal palygorskite (La-Al-HP)	1.30 mg/g	4.89 mg/L	540 min	7.5
6	Fe^{3+}-modified bentonite clay	2.91 mg/g	10 ppm	30 min	2~10
7	MnO_2 coated Na-bentonite	2.4 mg/g	5 mg/L	30 min	8
8	Hydroxyapatite nanorods	1.49 mg/g	10 mg/L	3 h	7
9	Sulfate-doped hydroxyapatite hierarchical hollow microspheres	28.3 mg/g	2–100 mg/L	2 h	3.0~10.0
10	Hydroxyapatite decorated with carbon nanotube composite (CNT-HAP)	11.05 mg/g	15 mg/L	300 min	6
11	Hydroxyapatite montmorillonite (HAP-MMT)	16.7 mg/g	30 mg/L	30 min	5
12	Zirconium impregnated activated carbon (ZrAC)	5.4 mg/g	2.5–20 mg/L	180 min	4
13	Mg-Mn-Zr impregnated activated carbon (ACMg-Mn-Zr)	26.27 mg/g	5–30 mg/L	3 h	4
14	Alumina impregnated activated carbon	2.86 mg/g	10 mg/L	3 h	6.1
15	Activated alumina	-	2–20 mg/L	24 h	6~8
16	Acid activated alumina	69.52 mg/g	10–60 mg/L	3 h	6.5
17	Nitric acid activated alumina	45.75 mg/g	40 mg/L	3 h	3.5

2. Materials and Methods

2.1. Chemicals

In this study, AA, sodium fluoride (NaF), ammonia ($NH_3 \cdot H_2O$), ammonium ferrous sulfate ($(NH_4)_2Fe(SO_4)_2 \cdot 6H_2O$) and hydroxylamine hydrochloride (H_4ClNO) were purchased from Sinopharm Chemical Reagent Co., Ltd. (CHN). Aluminum sulfate ($Al_2(SO_4)_3$), manganese sulfate ($MnSO_4$), hydrochloric acid (HCl), phenanthroline ($C_{12}H_8N_2$), ammonium acetate (CH_3COONH_4) and glacial acetic acid (CH_3COOH) were provided by Tianjin Kemiou Chemical Reagent Co., Ltd. (CHN). Hydrogen peroxide (H_2O_2) and SPADNS reagent were purchased from Tianjin Damao Chemical Reagent Factory (CHN) and America HACH company (USA), respectively. As shown in Table 3, a fluoride solution was prepared by dissolving a certain amount of NaF and $(NH_4)_2Fe(SO_4)_2 \cdot 6H_2O$ in deionized water (DI water). Note that the actual initial concentration of the pollutant solution is subject to the actual measured value on that day. All chemicals were all of analytical grade and DI water (resistivity of 18.2 MΩ·cm) was used in all experiments.

Table 3. Reference sample preparation.

	F^-	Total Fe
Concentration (mg/L)	2 ± 0.5	2 ± 0.5
	5 ± 0.5	2 ± 0.5
	10 ± 0.5	2 ± 0.5

2.2. Fabrication of MnOOH-Supported AA

2.2.1. Modification of AA

As shown in Figure 1a, 100 g of AA particles was added in 200 mL of an $Al_2(SO_4)_3$ solution with a concentration of 4%. Subsequently, the solutions were mixed for 24 h at a speed of 120 r/min. After that, the obtained solutions were washed with DI water several times until the pH of the effluent was stable, then dried in an oven for 2 h at 103 °C. The modified AA was used after cooling to room temperature. It was noteworthy that SO_4^{2-} in the solution could combine with AA by electrostatic or chemical adsorption, forming sulfate-type AA. The chemical reaction is expressed as follows:

$$(Al_2O_3)_n \cdot 2H_2O + SO_4^{2-} \rightarrow (Al_2O_3)_n \cdot H_2SO_4 + 2OH^- \quad (1)$$

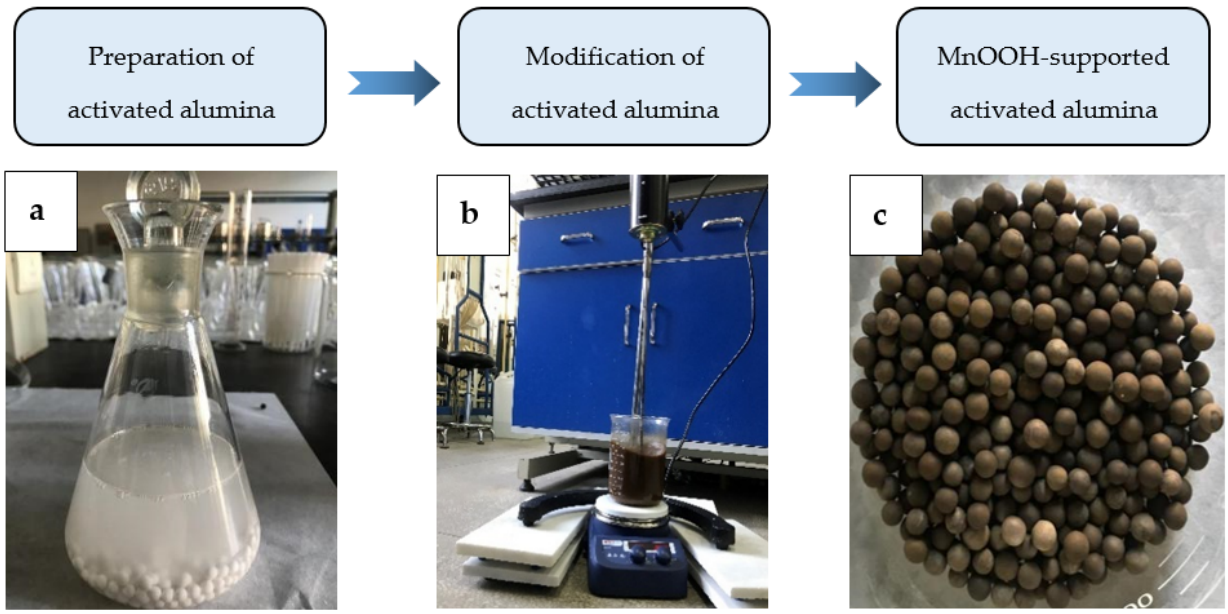

Figure 1. Schematic diagram for the preparation process of MnOOH-supported AA.

2.2.2. AA Coated with MnOOH

Figure 1b shows that MnOOH-supported AA was fabricated using an impregnation method. Firstly, 50 g of the modified AA particles was dispersed in 250 mL of a $MnSO_4$ solution (0.06 mol/L). Thereafter, the mixture was continuously stirred, injected with 5.1 mL of H_2O_2 with a concentration of 30%, and heated to 95 °C. Next, 75 mL of 0.2 mol/L $NH_3 \cdot H_2O$ was poured into the above solution. The brown precipitates generated on the surface of AA were MnOOH. To increase the contact area, the as-obtained mixture was continuously stirred at 165 r/min for 6 h. After that, the samples were firstly dried at 100 °C for 2 h, then washed thoroughly 8 times with 70–80 °C hot DI water, and finally dried for 4 h at 100 °C. As presented in Figure 1c, the MnOOH-supported AA was cooled in an indoor environment naturally for further use.

2.3. Adsorption Experiment

The adsorption kinetic experiment was carried out as follows: 200 mL of a fluoride solution was treated with the addition of a certain amount of MnOOH-supported AA at pH 4 and a temperature of 25 °C. The mixture was then oscillated at a moderate speed of 120 r/min using a thermostatic oscillator. To reduce variations, measurements were conducted in three parallel experiments, and the results presented were the average values. The adsorption kinetic model on MnOOH-supported AA was established on the basis of the experimental data.

With respect to the adsorption thermodynamic experiment, 7 g/L of MnOOH-supported AA was added into the fluoride solution at pH 4 and oscillated for 12 h to attain adsorption/desorption equilibrium. The initial concentrations of the fluoride solution were 2, 5, 10, 15 and 20 mg/L. In addition, the iron ion content was 2 mg/L. To study the effect of temperature on adsorption, the temperatures were controlled at 25 °C, 35 °C and 45 °C. The adsorption thermodynamic model was established, and the thermodynamic parameters of the adsorption process were also calculated. The mechanism of fluoride adsorption on MnOOH-supported AA was further discussed.

2.4. Mathematical Model and Basic Parameter Expression

2.4.1. Adsorption Kinetic Model

To get insight into the adsorption properties and rate-limiting step during the adsorption process, the adsorption kinetics of fluoride were investigated with a quasi-first-order model, a quasi-second-order model [21] and the Weber and Morris model [22,23]. The mathematical expressions are shown as Equations (2)–(4).

$$ln(q_e - q_t) = lnq_e - k_1 t \quad (2)$$

$$\frac{t}{q_t} = \frac{1}{k_2 {q_e}^2} + \frac{t}{q_e} \quad (3)$$

$$q_t = k_p t^{1/2} + C \quad (4)$$

where q_e and q_t (mg/g) represent the adsorption quantity at equilibrium and time, respectively; k_1 and k_2 are the rate constant of the quasi-first-order reaction and the quasi-second-order reaction, respectively; k_p (mg/(g·min$^{1/2}$)) represents the particle diffusion rate constant; t (min) is the adsorption time and C is a constant which characterizes the extent of diffusion.

2.4.2. Adsorption Thermodynamic Model

The Langmuir isotherm model and Freundlich isotherm model were applied to fit the equilibrium adsorption data. The Langmuir and Freundlich models are shown as Equations (5) and (6):

$$\frac{C_e}{q_e} = \frac{C_e}{q_{max} \frac{1}{K_L q_{max}}} \quad (5)$$

$$lnq_e = lnK_F + \frac{1}{n} lnC_e \quad (6)$$

where q_{max} (mg/g) represents the maximum adsorption capacity, C_e (mg/L) is the concentration of adsorbate at equilibrium, K_L is the Langmuir constant, K_F is the Freundlich constant, n refers to a measure of adsorption intensity ($1/n$ = 0.5~1, the adsorption process is conducted easily; $1/n > 2$, the adsorption process is arduous) [24].

2.4.3. Adsorption Thermodynamic Parameters

To better expound the adsorption mechanism, the adsorption thermodynamic parameters, i.e., adsorption enthalpy (ΔH), adsorption free energy (ΔG) and adsorption entropy (ΔS), were assessed.

ΔH could be calculated through the Van't Hoff equation, as shown in Equation (7):

$$ln\frac{1}{C_e} = -\frac{\Delta H}{RT} + lnK_0 \quad (7)$$

where ΔH (kJ/mol) is the isosteric enthalpy variation of adsorption, C_e (mol/L) is the equilibrium concentration of the solution at the absolute temperature T (K), R is the gas constant (8.314 J/(mol·K)) and K_0 is the equilibrium adsorption distribution coefficient.

ΔG can be obtained with the Gibbs free energy equation. If the adsorption isotherm can be described using the Freundlich equation model, the ΔG obtained is independent of q when the mass concentration of the adsorbate is low, expressed as follows:

$$\Delta G = -nRT \quad (8)$$

where ΔG (kJ/mol) is the change of adsorption free energy and n is the Freundlich exponent.

ΔS could be obtained using the Gibbs–Helmholtz equation, as shown in Equation (9):

$$\Delta S = \frac{\Delta H - \Delta G}{T} \quad (9)$$

2.5. Analytical Methods

The water quality indexes were detected by the Standard Test Method for Drinking Water (GB/T 57750-2006). The detection and analysis method, and standard limits for drinking water are displayed in Table 4. The surface morphology of MnOOH-supported AA was observed by scanning electron microscopy coupled with energy dispersive X-ray spectrometry (SEM-EDS) (S-4800, Hitachi, Japan), and the photomicrographs were recorded at an acceleration voltage of 5 kV and a constant temperature. The specific surface was measured by N_2 air-suction desorption on an automatic static physical adsorption instrument (Autosorb-IQ2-MP, Quantachrome, America). The total specific surface was calculated based on the multi-point Brunauer, Emmentt and Teller equation (P/P_0 = 0.005–0.3) with point range of 30 points for adsorption and 30 points of desorption. X-ray photoelectron spectra (XPS) were measured utilizing ESCALAB 250Xi (Thermo Fisher Scientific, China) with an Al (hv = 1486 eV) X-ray source at the standard mode. Prior to measurement, conductive tape was stuck on the tinfoil, and the sample powder was evenly spread on the surface of conductive tape. The sample surface was then covered with flat tinfoil, which was placed on the table press at a pressure of 1.5 T for 1 min. Lastly, the sample sheet was placed on the sample table to determine the XPS spectra. Fourier-transform infrared spectrometry (FTIR) (NICOLET iS50, Thermo Nicolet Corporation, America) was applied to analyze the infrared adsorption spectroscopy in transmission mode. Specifically, 10 mg of the sample was mixed evenly with 500 mg of potassium bromide powder using a sample mixer and compressed into a thin slice for examination. The infrared range was set to 4000–400 cm^{-1} and each scan was checked 32 times.

Table 4. Experiment detection method.

Test Item	Detection and Analysis Method	Standard Limits for Drinking Water (mg/L)
F^-	Fluorometric spectrophotometry	1.0
Fe	Phenanthroline spectrophotometry	0.3
T	Direct-reading method	-

3. Results

3.1. Characterization of MnOOH-Supported AA

3.1.1. Surface Morphology and Phase Composition

It is well known that the adsorption reaction on the particle surfaces is directly affected by the surface morphology. Hence, the surface morphologies of three kinds of AA were directly observed by SEM, as depicted in Figure 2. It was discovered that the surface appearance of modified AA was markedly different from ordinary AA. To be specific, obvious bulks were heaped up on the ordinary AA surface, and the porous structure was also inconspicuous. By contrast, the pre-treated AA had a certain pore structure, which contributed to fluoride adsorption. This phenomenon could be explained by the fact that the impurities present in AA were removed by the modification, leading to an increase of porosity. It can be seen in Figure 2b that the surface of MnOOH-supported AA formed an irregular and convex spinous structure. It was noticed that a well-developed pore structure was achieved, which was consistent with the finding of Wang et al. [25]. Meanwhile, the EDS analysis in Figure 3 indicates that MnOOH-supported AA clearly had more surface oxygen content than the ordinary AA, and a small amount of Mn element was also observed. To this end, it can be concluded that MnOOH was successfully loaded on the AA surface. Apparently, better dispersion of MnOOH could be achieved, and the surface of MnOOH-supported AA was rougher than that of the original AA, resulting in excellent adsorption ability. As compared with the unmodified AA, the specific surface of MnOOH-supported AA increased from 2.684 m^2/g to 3.311 m^2/g, and MnOOH-supported AA contained a range of pores with different sizes, exhibiting better porosity properties. The above results showed that the MnOOH-supported AA with a large amount of adsorption sites enhanced the fluoride adsorption capacity.

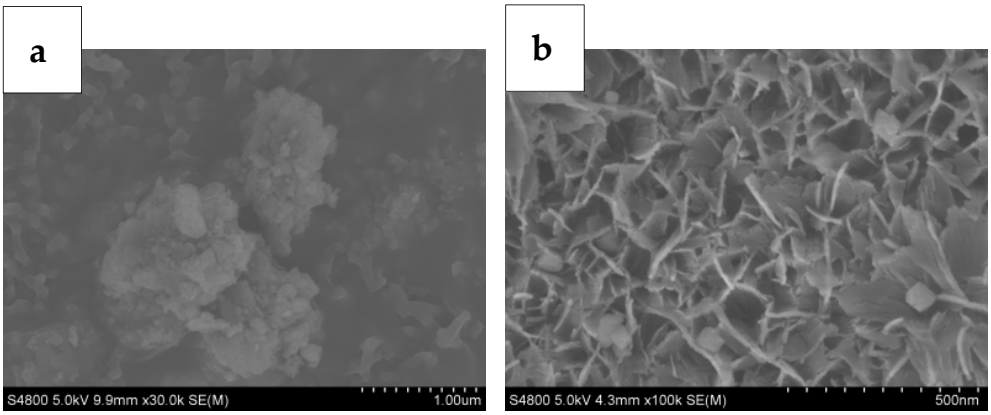

Figure 2. SEM images of fresh AA (**a**) and MnOOH-supported AA (**b**).

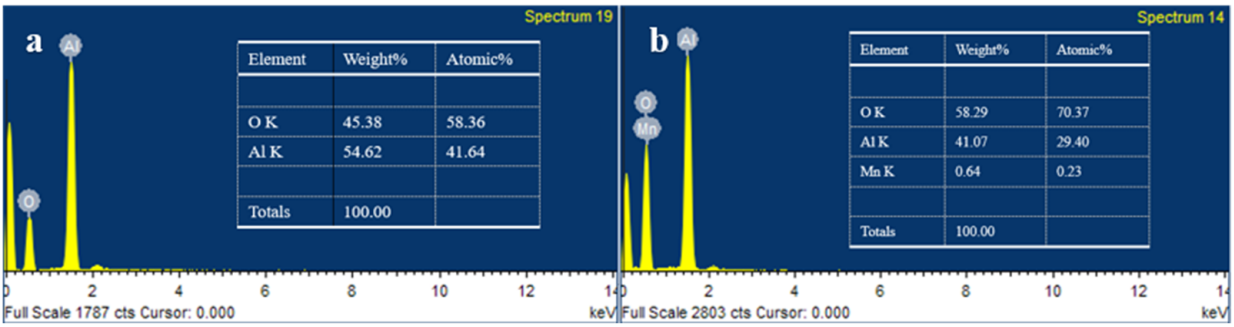

Figure 3. EDS results of AA (**a**) and MnOOH-supported AA particles (**b**).

3.1.2. XPS Analysis

The XPS spectra of AA before and after modification are presented in Figure 4. It can be clearly observed that the elements O, Al and Mn were the main constituent elements of MnOOH-supported AA, consistent with the results of EDS. In addition, the XPS peak-fitting analysis for the Mn2p peak of MnOOH-supported AA is shown in Figure 5. Apparently, the Mn2p band in the MnOOH-supported AA was mainly composed of two pinnacles: the MnOOH peak at 641.5 eV and the MnO peak at 653.4 eV, accounting for 59.2% and 40.7% respectively. These results revealed that the surface of AA was successfully loaded with MnOOH.

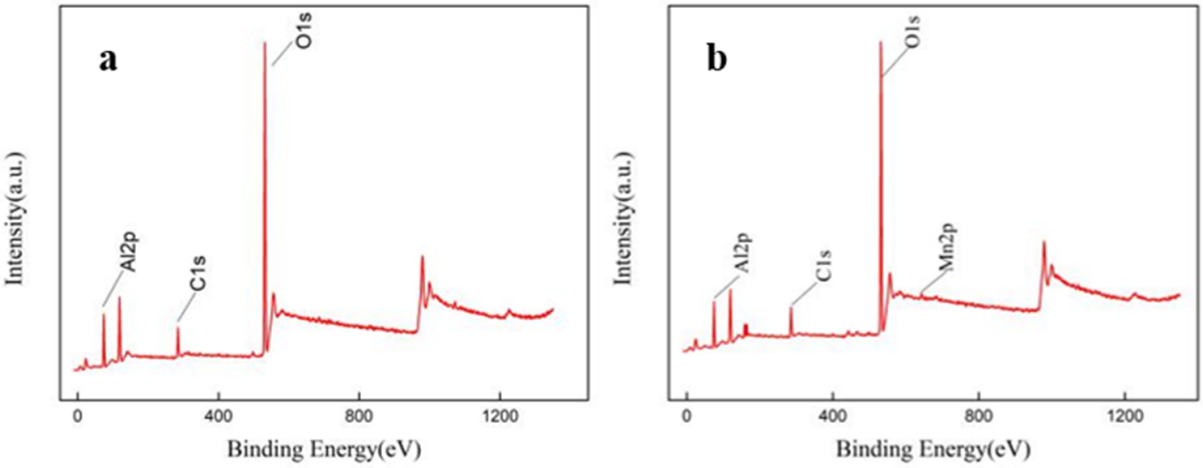

Figure 4. XPS pattern of AA (**a**) and MnOOH-supported AA particles (**b**).

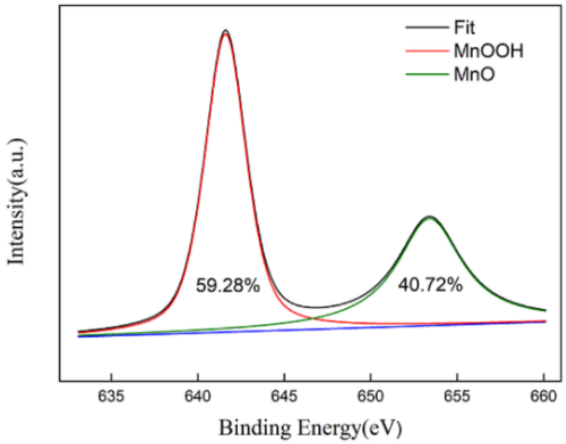

Figure 5. XPS peak-fitting analysis for the Mn2p peak of MnOOH-supported AA.

3.1.3. FTIR

The typical FTIR spectra of AA and MnOOH-supported AA are shown in Figure 6. The -OH stretching vibration at 3455.84 cm^{-1}, H_2O bending vibration at 1617 cm^{-1}, and CO_3^{2-} symmetric stretching vibration at 1384.44 cm^{-1} are clearly observed. The reasonable explanation for this phenomenon was that AA with a large surface area and hydrophilicity inevitably absorbed H_2O and CO_2 in the air. Note that the low peak values corresponding to H_2O and CO_2 vibration were observed, implying low contents of H_2O and CO_2 in the adsorbent. The typical peak at 605.64 cm^{-1} was attributed to Al-O bond vibration in unmodified AA, while a higher peak at 586.84 cm^{-1} was noticed in MnOOH-supported AA due to the combination of Al-O and Mo-O bonds. The above results revealed that there was little variation in the functional groups of MnOOH-supported AA as compared with the control; however, an increased -OH stretching vibration peak was obtained. Hence, the content of -OH was enhanced, which provided more adsorption sites for defluoridation.

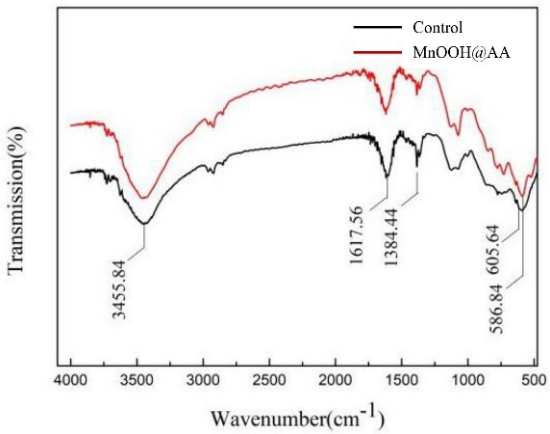

Figure 6. FTIR of AA before and after modification.

3.2. Analysis of Influential Factors and Regeneration Effects

3.2.1. Effect of MnOOH-Supported AA on Fluoride Removal

Figure 7 depicts the effects of AA before and after modification on fluoride removal. For both MnOOH-supported AA and the original AA, the performance of defluoridation was improved with an increase in dosages. Specifically, with 1 g/L of the adsorbent treatment, the removal rates of AA and MnOOH-supported AA were 8.41% and 15.4%, respectively. When 15 g/L of AA and MnOOH-supported AA was added, respectively, the reduction rates were 31.75% and 73.33%. As compared with AA, it appeared that MnOOH-supported AA displayed superior fluoride removal performance, with the defluoridation rate doubled.

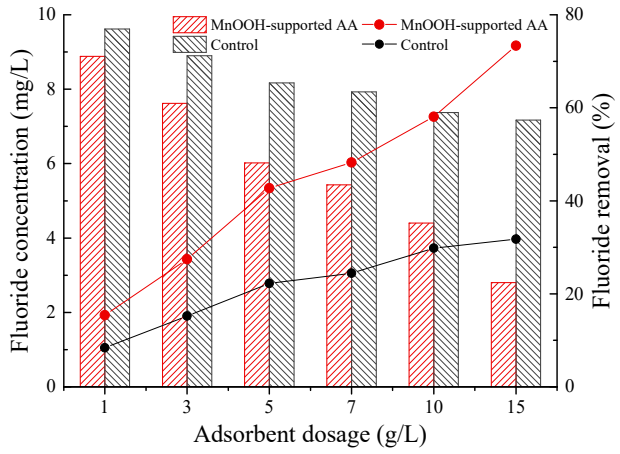

Figure 7. Effect of the MnOOH-supported AA and AA on defluoridation.

On the one hand, an irregular and convex spiny structure was seen on the surface of MnOOH-supported AA particles. The special structure provided more active sites for adsorption reactions [26], hence increasing the reduction efficiency of fluoride. On the other hand, when MnOOH-supported AA was dispersed in the solution, the ions located on the adsorbent surface were stressed unevenly due to the internal and surface forces of the particles, causing ions to have interface energy [27]. To reduce the interface energy, MnOOH-supported AA underwent surface hydroxylation by absorbing water molecules [19] and MnOOH reverted to $Mn(OH)_2$. Simultaneously, the surface of MnOOH-supported AA was covered by a certain amount of hydroxide radicals [28], thereby increasing the active sites for removing fluoride [29]. Since OH^- and F^- with a similar hydrate ionic radius can occur ionic coordination reaction in an acidic solution, fluoride was removed through the exchange of hydroxyl groups on the adsorbent surface [30]. The chemical reaction equations are shown as follows:

$$(Al_2O_3)_n \cdot MnOOH + H_2O \rightarrow (Al_2O_3)_n \cdot Mn(OH)_2 + OH^- \quad (10)$$

$$R - (Al_2O_3)_n \cdot Mn(OH)_2 + 2F^- \rightarrow R - (Al_2O_3)_n \cdot MnF_2 + 2OH^- \quad (11)$$

In addition, an underground hot spring water in Liaoning Province was used to investigate the fluoride removal performance. As can be seen in Table S1, under the condition of 5.6 mg/L of F^- concentration and 7 g/L of the adsorbent, the removal rates of AA and MnOOH-supported AA were 37.72% and 67.75%, respectively. It was concluded that MnOOH-supported AA had a better fluoride removal effect than AA, and the fluoride removal rate was increased by more than 70%.

3.2.2. Effect of pH on Fluoride Adsorption

The effect of pH on fluoride removal was investigated, and the results are shown in Figure 8. Obviously, the fluoride removal effect decreased with the increase in pH values. Specifically, with the F^- concentration increasing from 2 to 5 mg/L, the F^- adsorption capacity increased from 0.16 to 0.41 mg/g, and the removal rate was promoted from 77.09~80.3% to 80.85~83.27%. Based on these results, a pH of 4 was determined for the thermodynamic and kinetic studies.

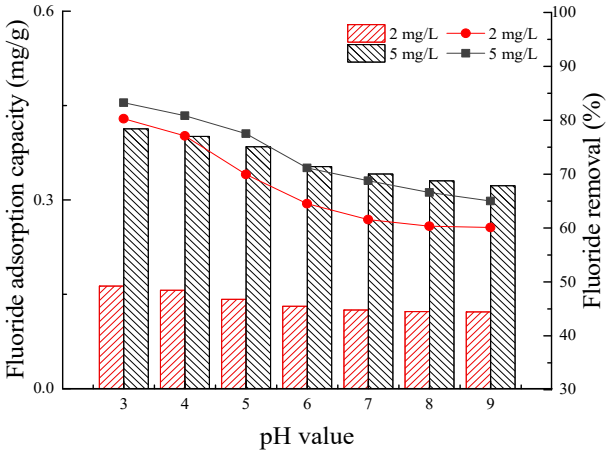

Figure 8. Effect of pH on fluoride removal by MnOOH-supported AA.

Meanwhile, the fluoride removal effects of MnOOH-supported AA with a particle size of 0.5–1.5 mm under different pH conditions were compared and analyzed. As shown in Figure S2, the fluoride removal rate and adsorption amount of the adsorbent gradually decreased with the increase in pH. Under acidic pH conditions, the fluoride removal effect of the system was better. It can also be seen in these results that the fluoride removal effect of small particles was significantly better than that of large particles.

3.2.3. Effect of Coexisting Anions on Fluoride Adsorption

Figure 9 describes the effects of coexisting anions on the fluoride adsorption of MnOOH-supported AA and AA. As shown in Figure 9a, there were various effects of coexisting anions on F^- removal by MnOOH-supported AA. The F^- removal performance was greatly affected by carbonate, while a slight impact was produced by chloride and nitrate. Specifically, the removal rates were reduced from 22.89% to 0.5% due to carbonate, and bicarbonate resulted in a decrease in the removal rate from 24.88% to 18.41%. This was mainly owing to the competitive adsorption between interfering anions and F^-, leading to a reduction in the adsorption effect. It can be seen from Figure 9b that the removal rate decreased with an increasing concentration of interfering anions. The effect of bicarbonate and sulfate on fluoride removal decreased from 16.92% to 1% and 29.35% to 15.42%, respectively.

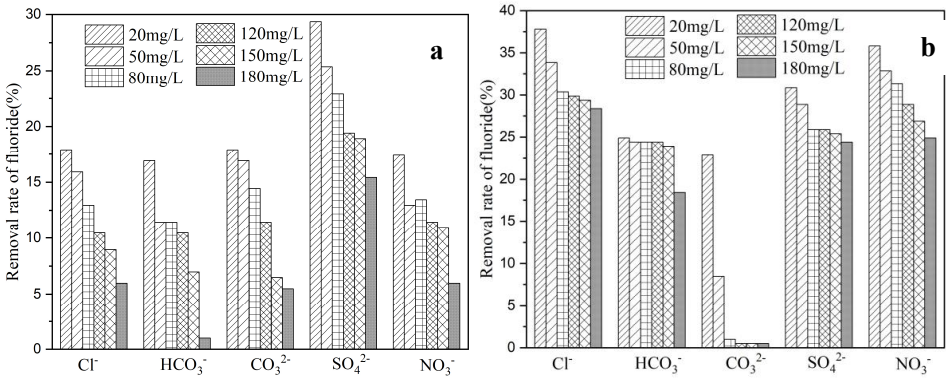

Figure 9. Effect of coexisting anions on F^- adsorption by MnOOH-supported AA (**a**) and AA (**b**).

3.2.4. Regeneration of MnOOH-Supported AA

The MnOOH-supported AA was regenerated using the acid-base regeneration process, and the results are shown in Tables 5 and 6. Here, 2.5% Na_2CO_3 was selected as the regenerating agent to obtain the greatest effect. Firstly, a certain amount of MnOOH-supported AA was regenerated, followed by 0.2 mol/L H_2SO_4 pickling for 0.5 h; finally, it was dried after washing with distilled water for 0.5 h. It was concluded that the effluent mass concentration of F^- of MnOOH-supported AA was 0.96 mg/L after regeneration for 2 h and the removal rate reached 80.8%. Compared with the first removal effects, the removal rate of fluoride ions decreased by 0.2%.

Table 5. Influence of regenerant concentration on regeneration effects (Na_2CO_3).

Regenerant Concentration (mg/L)	F^- Concentration (mg/L)	Removal Rate (%)
1	2.48	50.40
2	1.32	73.60
2.5	1	80.16
5	0.98	80.56
7.5	0.97	80.75
10	0.96	80.95

Table 6. Influence of regenerant time on regeneration effects (Na_2CO_3).

Regenerant Time (h)	F^- Concentration (mg/L)	Removal Rate (%)
1	1.17	76.79
1.5	1.13	77.58
2	0.96	80.8
2.5	1.17	76.79
3	1.45	71.23

3.3. Kinetic Study of Fluoride Adsorption

3.3.1. Quasi-First-Order Model and Quasi-Second-Order Model

The adsorption dynamic curves under different initial mass concentrations of fluoride are displayed in Figure 10. It is worth noting that a similar variation tendency of the adsorption rate curve was observed while treating different raw water. The adsorbed amount rapidly increased in 600 min of adsorption time, irrespective of the dosage. This could be ascribed to the fact that MnOOH-supported AA possessed rich active sites, leading to a rapid transformation of F^- from the solution to the surface. It was clear that the adsorption of fluoride was mainly external diffusion in the initial adsorption process. Subsequently, the adsorption sites were gradually covered by fluoride with an increase in adsorption time, and the solvent diffusion rate slowed down accordingly. After that, the defluoridation primarily occurred in the internal pores of particles. F^- diffused from the outer surface of particles to the inner surface of micropore when the adsorption time increased from 600 min to 1500 min. With the extension of adsorption time, the adsorbed amount slowly increased until it tended to be stable. In an adsorption time of over 1500 min, the adsorption sites in the surface and inner pores were all occupied. At this moment, the adsorption of fluoride on MnOOH-supported AA came to an equilibrium state.

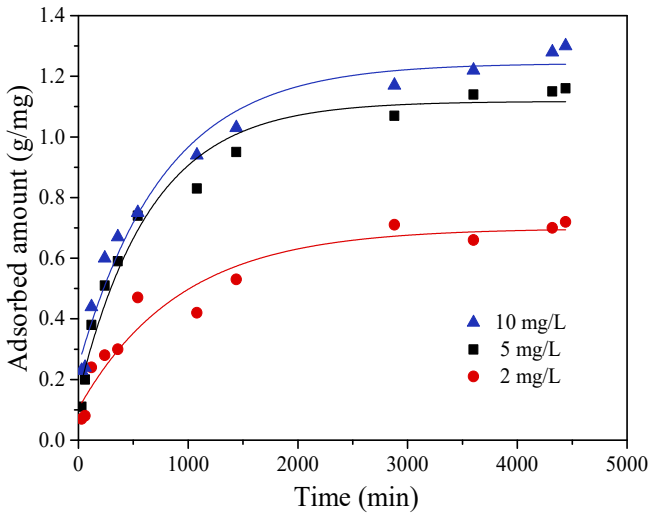

Figure 10. Adsorption dynamic curve of fluoride on MnOOH-supported AA.

Figure 11 presents the kinetic curves of fluoride with initial concentrations of 2, 5 and 10 mg/L for adsorption on MnOOH-supported AA. The correlation coefficients (R^2) were 0.8060, 0.9764 and 0.9632 as evaluated by the quasi-first-order model (Figure 11a). According to the quasi-second-order model, the R^2 values were 0.9862, 0.9978 and 0.9956, respectively (Figure 11b). It could be discovered that the experimental data perfectly fitted with the quasi-second-order equation. The results demonstrated that the quasi-second-order model could describe the entire defluoridation process, which was in accordance with previous studies [20,27,31]. During the adsorption process, some fluoride passed through the orifice and diffused into the pores of MnOOH-supported AA, which was described as physical adsorption. Some other fluoride was adsorbed owing to the fluoride–hydroxyl exchange reaction, which was chemical adsorption. Therefore, the adsorption process of fluoride was composed of physical adsorption and chemical adsorption, and chemical adsorption played the dominant role. In general, the entire defluoridation kinetics of MnOOH-supported AA were better fitted by the quasi-second-order model [32,33], including external diffusion, inner diffusion, and surface adsorption, etc. [34].

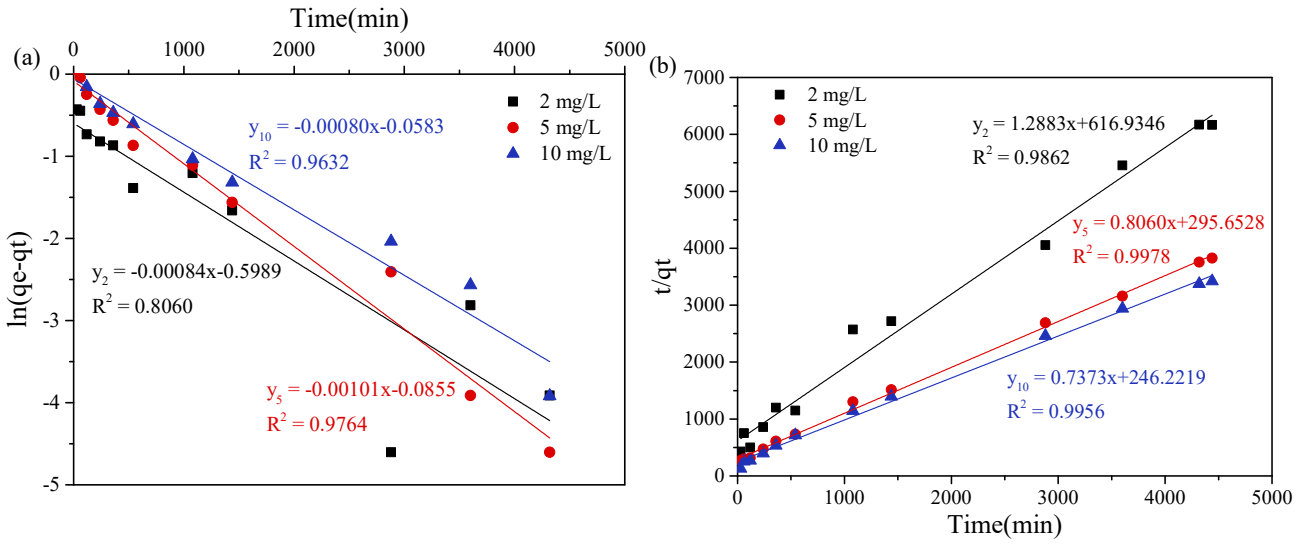

Figure 11. Fitting of the fluoride adsorption process with the quasi-first-order kinetics model (**a**) and the quasi-second-order kinetics model (**b**).

3.3.2. Weber and Morris Model

Though the quasi-second-order model could describe the entire adsorption process well, the intra-particle diffusion was not well assessed. Thus, the Weber and Morris model was used to further analyze the inner diffusion effect [22]. Figure 12 exhibits the plots of q_t versus t for initial concentrations of 2, 5 and 10 mg/L. Saini et al. [35] reported that the main rate-limiting reaction was intra-particle diffusion when the curve of q_t versus $t^{1/2}$ went through the origin and presented favorable linear relationships. In Figure 12, irrespective of the initial concentration, the fit lines are straight and distinct inflection points appear at 23 $min^{1/2}$. What is noteworthy is that all fit lines never pass through the origin. The results revealed that the adsorption rate was controlled not only by intra-particle diffusion but also by external diffusion. Specifically, the first (0~23 $min^{1/2}$) and the second (23~67 $min^{1/2}$) adsorption processes were assigned to external diffusion and intra-particle diffusion, respectively. the parameters of the Weber and Morris equation are listed in Table 7. As seen, the linear correlation of MnOOH-supported AA on fluoride was relatively preferable in the entire first adsorption process (0~23 $min^{1/2}$). This could imply that the reaction was mainly controlled by external diffusion. For the second adsorption process (23~67 $min^{1/2}$), q_t and $t^{1/2}$ also showed a relatively good linear relationship, though R^2 was lower than that of the first adsorption process. It can be concluded from the C and k values that diffusion in this stage was chiefly dependent on the internal diffusion rate. The above results indicated that defluoridation using MnOOH-supported AA was the common result of external and intra-particle diffusion.

Table 7. Parameters of the Weber and Morris model.

C^0 (mg/L)	0~23 $min^{1/2}$			23~67 $min^{1/2}$		
	R^2	k	C	R^2	k	C
2	0.9112	0.0212	−0.0494	0.8294	0.0067	0.2738
5	0.9789	0.0347	−0.0524	0.9658	0.0097	0.5357
10	0.9494	0.0318	−0.0548	0.9648	0.0116	0.5372

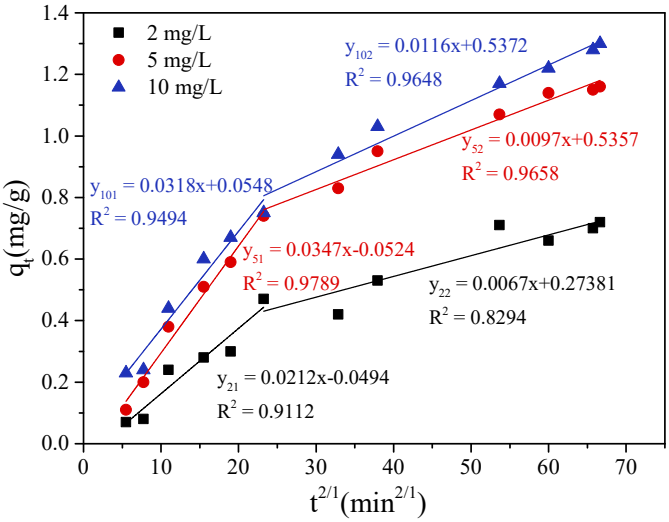

Figure 12. Fitting of the fluoride adsorption process with the Weber and Morris model.

3.4. Kinetic Study of Fluoride Adsorption

3.4.1. Adsorption Isotherms

In Figure 13, the variation trend of three is was basically the same in 25 °C, 35 °C and 45 °C. Significantly, the equilibrium adsorption capacity gradually increased with an increased initial concentration. Although the slope of curve was reduced, the unit adsorption capacity of MnOOH-supported AA improved constantly. This was mainly attributed to the fact that when the initial concentration of fluoride was relatively high, the solution concentration gradient increased on the inside and outside of particles. This was propitious to accelerate the diffusion rate and enlarge the equilibrium adsorption amount of fluoride [22].

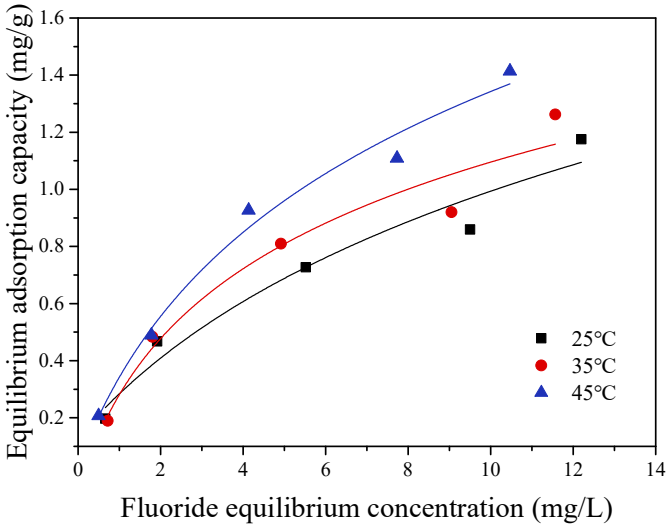

Figure 13. Adsorption isotherm curve of fluoride on MnOOH-supported AA.

To get insight into the adsorption thermodynamic characteristics of MnOOH-supported AA, the Langmuir adsorption isotherm was used to analyze the defluorination properties; the results are shown in Figure 14. The related parameters of the Langmuir model and the Freundlich model at different temperatures are seen in Table 8. It may be thought that the adsorption process of MnOOH-supported AA on fluoride was well explained using both the Langmuir and Freundlich isotherms. However, fluoride adsorption was more suitable for the Freundlich model, with R^2 values of 0.9614, 0.9383 and 0.9852 at

25 °C, 35 °C and 45 °C, respectively. In Table 8, the constant $1/n$ of the Freundlich equation is 0.5631, 0.6243 and 0.6241, which illustrated that adsorption was conducted easily in all cases. In addition, the K_F values increased with an increase in adsorption temperature, suggesting that high temperatures contributed to the adsorption of fluoride on MnOOH-supported AA. The K_L values were all positive under different temperatures, which accelerated the adsorption reaction. It was also observed that the K_L values were enlarged when temperature increased, suggesting a chemical adsorption mechanism for the reaction system. Overall, the Freundlich isotherm was applicable to the adsorption data of all temperatures.

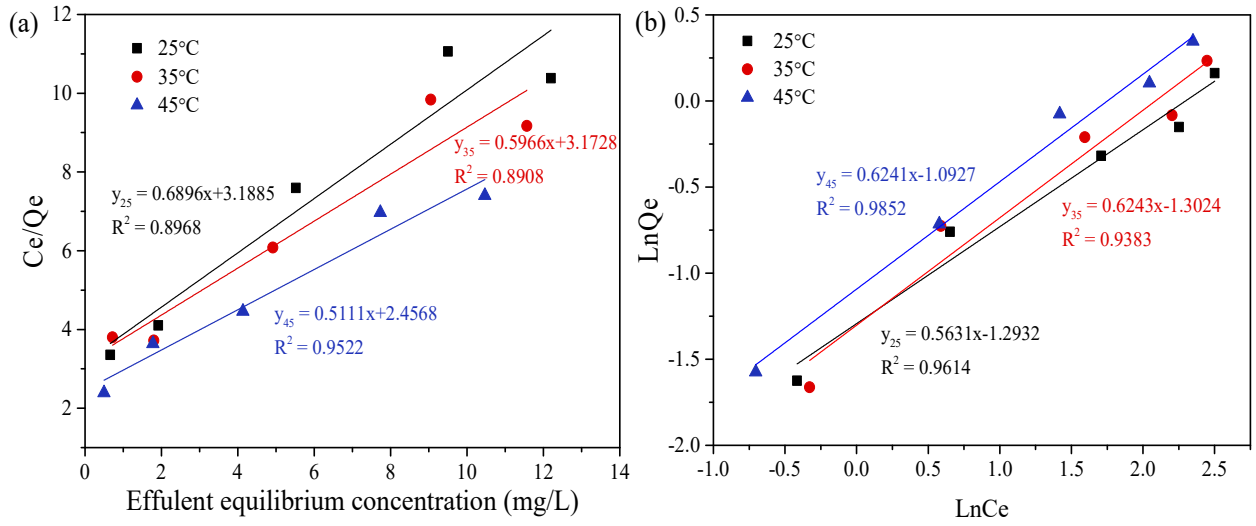

Figure 14. Fitting of the fluoride adsorption process with the Langmuir isotherm model (**a**) and the Freundlich isotherm model (**b**).

Table 8. Parameters of the adsorption isotherm models.

Temperature °C	Langmuir Model			Freundlich Model		
	K_L	q_e (mg/g)	R^2	K_F	$1/n$	R^2
25	0.216	1.450	0.8968	0.274	0.5631	0.9614
35	0.188	1.676	0.8908	0.272	0.6243	0.9383
45	0.208	1.957	0.9522	0.335	0.6241	0.9852

3.4.2. Isosteric Enthalpies for Adsorption

As different atoms and molecules were deposited on the surface, the surface energy of MnOOH-supported AA was unbalanced, thus generating Gibbs free energy. The defluoridation process was that MnOOH-supported AA absorbed several fluorides from the solution to balance its surface free energy. Along with the adsorption reaction, the Gibbs free energy slowly decreased and the surface energy came to a steady state [16,36]. As is well known, the adsorption free energy is the embodiment of the driving force. It can be seen from Table 9 that ΔG was less than zero at 25 °C, 35 °C and 45 °C, revealing that the adsorption reaction was spontaneous [37,38]. Meanwhile, ΔG gradually reduced with increasing temperature, which meant that the higher temperature was conducive to the progress of the adsorption reaction.

Through the analysis of adsorption isotherms, it was observed that improving the temperature was beneficial to the adsorption of fluoride on MnOOH-supported AA. The ΔH was greater than zero, which showed that the whole adsorption process was an endothermic reaction. The variation of ΔH during the adsorption process principally resulted from chemical reactions. The chemical reaction of fluoride on an adsorbent surface was mainly a displacement reaction with the activated hydroxyl group formed by the hydration

reaction. Generally, the increased temperature was not propitious to physisorption. This suggested that a chemisorption mechanism accorded with the defluoridation process onto MnOOH-supported AA.

Table 9. Thermodynamic parameters.

C_0 (mg/L)	ΔH (J/mol)	ΔG (J/mol)			ΔS (J/(mol·K))		
		298	308	318	298	308	318
2	11,131.61	−11,973.36	−12,375.15	−12,776.94	77.53	41.54	43.30
5	3004.26	−1408.50	−1455.76	−1503.03	14.81	4.89	5.05
10	11,370.23	−7110.14	−7348.73	−7587.33	62.01	24.67	25.52
15	8057.76	−2433.97	−2515.64	−2597.32	35.21	8.45	8.72

In addition, a positive Δ*S* higher than zero at three temperatures revealed an entropy production process for fluoride adsorption. During the adsorption process, the randomness of fluoride decreased and the confusion degree of the solid–liquid interface increased. This phenomenon could be explained by the fact that the exchange reaction between fluoride and water molecules on the adsorbent surface took place, leading to an improvement in the total Δ*S* in the entire system. We concluded that there was a preferable affinity between fluoride and MnOOH-supported AA. In the initial stage of the reaction, a great deal of heat was expended owing to the chemical reaction between fluoride and MnOOH-supported AA. As the coverage rate increased, active sites with high energy were gradually occupied and the amount of chemical reaction taking place was small. The fluoride adsorbed later was attached to the adsorption sites with low energy, causing less heat production.

4. Conclusions

(1) The surface of MnOOH-supported AA became rougher, exhibiting more adsorption sites and preferable porosity to enhance adsorption ability. The results obtained from XPS showed that the Mn2p peak of MnOOH-supported AA was composed of MnOOH at 641.5 eV and MnO at 653.4 eV, accounting for 59.2% and 40.7%, respectively, illustrating the ordinary AA was successfully loaded with MnOOH.

(2) The defluoridation kinetics of MnOOH-supported AA fitted well with the quasi-second-order model, with R^2 values of 0.9862, 0.9978 and 0.9956 in this present study. The adsorption process consisted of external diffusion, internal diffusion and chemical adsorption, among which, chemical adsorption was the primary adsorption mechanism. Additionally, the adsorption rate was governed by external diffusion and inter-particle diffusion conjointly, and the Weber and Morris diffusion was the main reason.

(3) The adsorption of fluoride onto MnOOH-supported AA was better fitted by the Freundlich isotherm, showing chemical adsorption processes. The results showed that both higher and lower temperature were favorable to improving the adsorption effects. During the entire defluoridation process, it was observed that Δ*S* and ΔH were all positive and ΔG was negative, illustrating a spontaneous and an endothermic diffusion adsorption mechanism.

Supplementary Materials: The following are available online at https://www.mdpi.com/article/10.3390/w13091219/s1. Table S1. Comparative analysis of fluoride removal methods. Figure S1. Distribution of areas with excessive fluoride and iron in groundwater in China, fluoride exceeded area (a) and iron exceeded area (b). Figure S2. Effect of pH on fluoride removal efficiency (Φ 0.5–1.5 mm).

Author Contributions: Data curation, K.Y. and N.K.; Formal analysis, N.K.; Funding acquisition, J.F.; Investigation, K.Y., N.K., Y.G., Y.Y. and F.Y.; Methodology, K.Y., X.C., Y.Y. and F.Y.; Project administration, J.F. and X.C.; Resources, J.F. and X.C.; Software, P.L. and Y.G.; Writing—original draft, K.Y.; Writing—review and editing, P.L. and X.C. All authors have read and agreed to the published version of the manuscript.

Funding: This research was funded by the Major Science and Technology Program for Water Pollution Control and Treatment, grant number "2018ZX070601001-3".

Data Availability Statement: Data are contained within the article.

Acknowledgments: This research was supported by the Major Science and Technology Program for Water Pollution Control and Treatment (2018ZX070601001-3).

Conflicts of Interest: The authors declare no conflict of interest.

References

1. Ranasinghe, N.; Kruger, E.; Tennant, M. Spatial distribution of groundwater fluoride levels and population at risk for dental caries and dental fluorosis in Sri Lanka. *Int. Dent. J.* **2019**, *69*, 295–302. [CrossRef]
2. Yan, J.; Chen, J.; Zhang, W.; Ma, F. Determining fluoride distribution and influencing factors in groundwater in Songyuan, Northeast China, using hydrochemical and isotopic methods. *J. Geochem. Explor.* **2020**, *217*, 106605. [CrossRef]
3. Jiang, K.; Zhou, K.; Yang, Y.; Du, H. A pilot-scale study of cryolite precipitation from high fluoride-containing wastewater in a reaction-separation integrated reactor. *J. Environ. Sci.* **2013**, *25*, 1331–1337. [CrossRef]
4. Jiang, K.; Zhou, K.; Yang, Y.; Du, H. Growth kinetics of calcium fluoride at high supersaturation in a fluidized bed reactor. *Environ. Technol.* **2013**, *35*, 82–88. [CrossRef]
5. Meenakshi; Maheshwari, R.C. Fluoride in drinking water and its removal. *J. Hazard. Mater.* **2006**, *137*, 456–463. [CrossRef] [PubMed]
6. Li, Q.; Wang, B.; Li, W.; Wang, C.; Zhou, Q.; Shuang, C.; Li, A. Performance evaluation of magnetic anion exchange resin removing fluoride. *J. Chem. Technol. Biotechnol.* **2015**, *91*, 1747–1754. [CrossRef]
7. Viswanathan, N.; Meenakshi, S. Role of metal ion incorporation in ion exchange resin on the selectivity of fluoride. *J. Hazard. Mater.* **2009**, *162*, 920–930. [CrossRef]
8. Boubakri, A.; Bouchrit, R.; Hafiane, A.; Bouguecha, S.A.-T. Fluoride removal from aqueous solution by direct contact membrane distillation: Theoretical and experimental studies. *Environ. Sci. Pollut. Res.* **2014**, *21*, 10493–10501. [CrossRef]
9. Sehn, P. Fluoride removal with extra low energy reverse osmosis membranes: Three years of large scale field experience in Finland. *Desalination* **2008**, *223*, 73–84. [CrossRef]
10. Arahman, N.; Mulyati, S.; Lubis, M.R.; Takagi, R.; Matsuyama, H. The removal of fluoride from water based on applied current and membrane types in electrodialyis. *J. Fluor. Chem.* **2016**, *191*, 97–102. [CrossRef]
11. Craig, L.; Stillings, L.L.; Decker, D.L. Assessing changes in the physico-chemical properties and fluoride adsorption capacity of activated alumina under varied conditions. *Appl. Geochem.* **2017**, *76*, 112–123. [CrossRef]
12. Dhawane, S.H.; Khan, A.A.; Singh, K.; Tripathi, A.; Hasda, R.; Halder, G. Insight into Optimization, isotherm, kinetics, and thermodynamics of fluoride adsorption onto activated alumina. *Environ. Prog. Sustain. Energy* **2017**, *37*, 766–776. [CrossRef]
13. Goswami, A.; Purkait, M.K. The defluoridation of water by acidic alumina. *Chem. Eng. Res. Des.* **2012**, *90*, 2316–2324. [CrossRef]
14. Viswanathan, N.; Meenakshi, S. Enriched fluoride sorption using alumina/chitosan composite. *J. Hazard. Mater.* **2010**, *178*, 226–232. [CrossRef] [PubMed]
15. Tripathy, S.S.; Bersillon, J.-L.; Gopal, K. Removal of fluoride from drinking water by adsorption onto alum-impregnated activated alumina. *Sep. Purif. Technol.* **2006**, *50*, 310–317. [CrossRef]
16. Kumari, U.; Behera, S.K.; Siddiqi, H.; Meikap, B. Facile method to synthesize efficient adsorbent from alumina by nitric acid activation: Batch scale defluoridation, kinetics, isotherm studies and implementation on industrial wastewater treatment. *J. Hazard. Mater.* **2020**, *381*, 120917. [CrossRef]
17. Kumari, U.; Siddiqi, H.; Bal, M.; Meikap, B. Calcium and zirconium modified acid activated alumina for adsorptive removal of fluoride: Performance evaluation, kinetics, isotherm, characterization and industrial wastewater treatment. *Adv. Powder Technol.* **2020**, *31*, 2045–2060. [CrossRef]
18. He, Y.; Zhang, L.; An, X.; Wan, G.; Zhu, W.; Luo, Y. Enhanced fluoride removal from water by rare earth (La and Ce) modified alumina: Adsorption isotherms, kinetics, thermodynamics and mechanism. *Sci. Total Environ.* **2019**, *688*, 184–198. [CrossRef]
19. Teng, S.-X.; Wang, S.-G.; Gong, W.-X.; Liu, X.-W.; Gao, B.-Y. Removal of fluoride by hydrous manganese oxide-coated alumina: Performance and mechanism. *J. Hazard. Mater.* **2009**, *168*, 1004–1011. [CrossRef]
20. Maliyekkal, S.M.; Sharma, A.K.; Philip, L. Manganese-oxide-coated alumina: A promising sorbent for defluoridation of water. *Water Res.* **2006**, *40*, 3497–3506. [CrossRef]
21. Ugya, A.Y.; Imam, T.S.; Hua, X.; Ma, J. Efficacy of Eichhornia Crassipes, Pistia Stratiotes and Nymphaea Lotus in the Biosorption of Nickel from Refinery Wastewater. *Appl. Ecol. Environ. Res.* **2019**, *17*, 13075–13087. [CrossRef]
22. Alemu, S.; Mulugeta, E.; Zewge, F.; Chandravanshi, B.S. Water defluoridation by aluminium oxide–manganese oxide composite material. *Environ. Technol.* **2014**, *35*, 1893–1903. [CrossRef] [PubMed]
23. Yang, C.; Gao, L.; Wang, Y.; Tian, X.; Komarneni, S. Fluoride removal by ordered and disordered mesoporous aluminas. *Microporous Mesoporous Mater.* **2014**, *197*, 156–163. [CrossRef]
24. Tseng, R.-L.; Wu, F.-C. Inferring the favorable adsorption level and the concurrent multi-stage process with the Freundlich constant. *J. Hazard. Mater.* **2008**, *155*, 277–287. [CrossRef] [PubMed]

25. Wang, L.; Duan, G.; Chen, S.-M.; Liu, X. Hydrothermally controlled synthesis of α-MnO2, γ-MnOOH, and Mn3O4 nanomaterials with enhanced electrochemical properties. *J. Alloys Compd.* **2018**, *752*, 123–132. [CrossRef]
26. Varghese, S.P.; Babu, A.T.; Babu, B.; Antony, R. Γ-Mnooh Nanorods: Efficient Adsorbent for Removal of Methylene Blue from Aqueous Solutions. *J. Water Process Eng.* **2017**, *19*, 1–7. [CrossRef]
27. Tripathy, S.S.; Raichur, A.M. Abatement of fluoride from water using manganese dioxide-coated activated alumina. *J. Hazard. Mater.* **2008**, *153*, 1043–1051. [CrossRef] [PubMed]
28. Mullick, A.; Neogi, S. Ultrasound assisted synthesis of Mg-Mn-Zr impregnated activated carbon for effective fluoride adsorption from water. *Ultrason. Sonochem.* **2019**, *50*, 126–137. [CrossRef]
29. Wen, T.; Zhong, H.; Pan, X.; Wang, P.; Wang, H.; Huang, L. Removal of Fluoride from Wastewater Solution Using Ce-Alooh with Oxalic Acid as Modification. *J. Hazard. Mater.* **2020**, *384*, 121373.
30. Huang, L.; Yang, Z.; Zhang, Z.; Jin, L.; Yang, W.; He, Y.; Ren, L.; Wang, H. Enhanced surface hydroxyl groups by using hydrogen peroxide on hollow tubular alumina for removing fluoride. *Microporous Mesoporous Mater.* **2020**, *297*, 110051. [CrossRef]
31. Ahamad, K.; Singh, R.; Baruah, I.; Choudhury, H.; Sharma, M. Equilibrium and kinetics modeling of fluoride adsorption onto activated alumina, alum and brick powder. *Groundw. Sustain. Dev.* **2018**, *7*, 452–458. [CrossRef]
32. Kumari, U.; Behera, S.K.; Meikap, B. A novel acid modified alumina adsorbent with enhanced defluoridation property: Kinetics, isotherm study and applicability on industrial wastewater. *J. Hazard. Mater.* **2019**, *365*, 868–882. [CrossRef]
33. Mariappan, R.; Vairamuthu, R.; Ganapathy, A. Use of chemically activated cotton nut shell carbon for the removal of fluoride contaminated drinking water: Kinetics evaluation. *Chin. J. Chem. Eng.* **2015**, *23*, 710–721. [CrossRef]
34. Simonin, J.-P. On the comparison of pseudo-first order and pseudo-second order rate laws in the modeling of adsorption kinetics. *Chem. Eng. J.* **2016**, *300*, 254–263. [CrossRef]
35. Saini, A.; Maheshwari, P.H.; Tripathy, S.S.; Waseem, S.; Dhakate, S. Processing of rice straw to derive carbon with efficient de-fluoridation properties for drinking water treatment. *J. Water Process. Eng.* **2020**, *34*, 101136. [CrossRef]
36. Li, R.; Tian, X.; Ashraf, I.; Chen, B. Fluoride removal using a chelating resin containing phosphonic-sulfonic acid bifunctional group. *J. Chromatogr. A* **2020**, *1613*, 460697. [CrossRef] [PubMed]
37. Roy, S.; Das, P.; Sengupta, S.; Manna, S. Calcium impregnated activated charcoal: Optimization and efficiency for the treatment of fluoride containing solution in batch and fixed bed reactor. *Process. Saf. Environ. Prot.* **2017**, *109*, 18–29. [CrossRef]
38. Ekka, B.; Dhaka, R.S.; Patel, R.K.; Dash, P. Fluoride removal in waters using ionic liquid-functionalized alumina as a novel adsorbent. *J. Clean. Prod.* **2017**, *151*, 303–318. [CrossRef]